Soft Matter

PAPER

Cite this: *Soft Matter*, 2017, **13**, 7264

Heat-controlled micropillar array device for microsystems technology†

Núria Torras, ‡§[a] Marcos Duque,‡[a] Carlos J. Camargo,[a] Jaume Esteve*[a] and Antoni Sánchez-Ferrer *[b]

Received 26th July 2017,
Accepted 18th September 2017

DOI: 10.1039/c7sm01480e

rsc.li/soft-matter-journal

A new temperature-controlled smart soft material micropillar array has been fabricated *via in situ* integration of the liquid-crystalline elastomer-based component into the hybrid microdevice. Such design allows for developing pushing elements with fast lifetime values of *ca.* 5 s, and opens huge opportunities for the use of hybrid smart microdevices with total control on the actuation time/response, repeatability, stability and energy saving.

Introduction

The integration of organic-based smart soft materials (*i.e.*, liquid-crystalline elastomers, LCEs) and inorganic-based engineered microstructures (*i.e.*, Microsystems Technology) leads towards the fabrication of a new generation of hybrid microdevices (*i.e.*, MEMS/MOEMS).[1]

LCEs are the combination of the liquid-crystalline anisotropic state of order and the entropy elasticity of a crosslinked polymer melt, which results in a material that changes its macroscopic dimensions if the liquid-crystalline molecules or mesogens are aligned and kept as a monodomain.[2] Such a change in shape can be promoted either when an external stimulus induces the local disorder of the mesogens – photo-isomerization with monochromatic light,[3,4] or reorientation with magnetic[5,6] or electric fields[7,8] – or when energy is absorbed by the material raising the material's temperature and reaching the isotropic state – increasing the temperature[9,10] or absorbing photons that undergo non-radiative processes.[11,12]

Integrating LCEs brings flexibility, processability and tunability to these new hybrid sensors or actuators, where external stimuli are applied and controlled by the microstructured support.[13] Several examples have already been described where two possible approaches – *ex situ* and *in situ* preparation of monodomains of LCEs – have been developed for the fabrication of such microdevices. A top-down approach (*ex situ* process) is thought for the integration of the LCE material into the final device previous shaping and alignment of the smart soft material (*e.g.*, micromotors,[14] microgrippers,[15] micropumps,[16] microvalves,[17] and Braille elements[18]), while a bottom-up approach (*in situ* process) is considered when shaping and alignment takes place during the integration process (*e.g.*, micropillars arrays,[19] actuators arrays,[20] photonic crystals,[21] Braille arrays,[22] and artificial iris[23]). Up to now, slow motions and high power dissipation process have been reported.

In this work, a successful nematic side-chain LCE micropillar array is presented, which expands in the direction of the applied orientation when the isotropic temperature is reached. Such an expansion is controlled by transferring heat, which is generated in the Au-microresistors placed at the bottom of each micropillar. Thermal-induced mechanical experiments have been performed on several LCE micropillars showing a maximal actuation force value of F = 32 mN after isotropization, and the presence of a fast (energy uptake) and a slow process (viscoelastic response), which lifetime values are as small as 5 and 16 s (upon heating) and 4 and 8 s (upon cooling), respectively. The perfect control of the LCE microdevice, which allows for minimizing the time response and energy dissipation, allows to envision a huge potential for new hybrid microdevice prototypes.

Experimental

Synthesis of the mesogen, crosslinker and the nematic side-chain liquid-crystalline elastomer micropillar array

The rod-like side-chain mesogen (SCM) and the isotropic sidechain crosslinker (SCC) were synthesized as described in previous

[a] *Instituto de Microelectrónica de Barcelona, IMB-CNM (CSIC), Campus UAB, Bellaterra, E-08193 Barcelona, Spain. E-mail: jaume.esteve@imb-cnm.csic.es*
[b] *ETH Zurich, Department of Health Sciences & Technology, IFNH, Schmelzbergstrasse 9, CH-8092 Zurich, Switzerland. E-mail: antoni.sanchez@hest.ethz.ch*

† Electronic supplementary information (ESI) available: Thermoelastic, mechanical, IR temperature, time dependent and cyclic experiment; *I–V* curve; setups description; and LCE modelling. See DOI: 10.1039/c7sm01480e

‡ The first two authors contributed equally to this study.

§ Present address: Institute for Bioengineering of Catalonia (IBEC), Barcelona Institute of Science and Technology (BIST), Baldiri Reixac 10-12, E-08028 Barcelona, Spain.

papers.[24–27] The oriented nematic LCE micropillar array was prepared using the compression orientational process, where both the mesogens and the polymer backbones show a planar orientation.[22] After the non-complete hydrosilylation reaction,[28,29] the sample was partially deswollen and removed from the reactor/mold and aligned by applying uniaxial compression perpendicular to the cylindrical axis. The curing process allowed the completion of the hydrosilylation reaction, while maintaining the compression of the sample – second step of the crosslinking reaction in the nematic phase during the orientation of the samples. The nematic LCE was synthesized using 20 mol% of crosslinking double bonds or 11.1 mol% of a crosslinker. For this crosslinking composition, the sample has 16 side-chain repeating units between two crosslinkers. In a 5 mL flask, 477 mg (1.60 mmol) of the side-chain mesogen (SCM) 4-methoxyphenyl 4-(but-3-en-1-yloxy)benzoate, 83 mg (0.20 mmol) of the isotropic side-chain crosslinker (SCC) 1,4-bis(undec-10-en-1-yloxy)benzene, and 120 mg (2.00 mmol SiH) of poly(methylhydrosiloxane) (PMHS, DP ∼ 259) were placed. To this mixture, 2 mL of thiophene-free toluene and 40 mL of 1%-Pt cyclooctadieneplatinum(II) chloride, $Pt(COD)Cl_2$, in dichloromethane were added. The reactive mixture was filled in the holes of the Teflon mold where at the bottom a Pyrex-treated support with the microstructured gold circuit was placed. The Pyrex support had in one face a gold printed circuit where a layer of allyl groups was produced after reacting the rest of the Pyrex surface with allyltrichlorosilane in order to enhance the adhesion of the LCE micropillars to the final device. Then, the entire mold was heated at 70 °C in an oven for 1 h 45 min. Afterwards, the reactor/mold was cooled and the elastomer micropillar array was removed. In this first step, the elastomer is not totally crosslinked. Some pressure was applied by fixing the distance between two Teflon plates in order to align the sample during the deswelling process, and in order to fix this orientation, the crosslinking reaction was completed by leaving the elastomer in the oven under a vacuum at 70 °C for 2 days.

Apparatus and techniques

Au-microresistors fabrication. Pyrex wafers of 100 mm diameter and 700 μm thickness from Präzisions Glas & Optic GmbH were used as a substrate for the fabrication of the Au-microresistors. A 2.0 μm-thick positive photoresist layer made out of ma-P 6512 from Micro Resist Technology was spin-coated on top. The layer was exposed to UV light (λ = 365 nm) through a photomask containing the designs and the final resist was hard baked during 10 min at 115 °C. A 10 nm-thick titanium–nickel (Ti–Ni) bilayer was first deposited, followed by the sputtering of a 50 nm-thick gold (Au) layer MRC 903 from Materials Research Corporation on top. Then, the processed wafer was immersed in acetone and ultrasounds were applied in order to remove the non-desired parts of metals (Ti–Ni and Au) and the remaining photoresist, leading to the corresponding resistors. Finally, the Au-microresistors were cut into individual chips and their top surface treated by depositing few drops of the reactive allyltrichlorosilane (95%) from ABCR under nitrogen atmosphere in order to guarantee a strong chemical adhesion of the LCE micropillars to the substrate.

LCE micropillar array fabrication. The templates for the LCE micropillars were micromechanized in Teflon to avoid any degradation during the evaporation of solvents and at high temperatures. The dimensions of the holes in the Teflon templates were calculated taking into account the volume fraction of non-volatiles which are the constituents of the final LCE micropillar. Some 30 mm side square Pyrex substrates with 0.5 mm thickness were chosen to ensure good heat transfer to the LCE micropillars. The deformation of the LCE micropillars was induced by applying a homogeneous uniaxial compression along the vertical axis of the LCE micropillars before the final crosslinking process of the material. Thus, from the original height of 4.20 mm after the first crosslinking stage, the micropillars were uniaxially deformed to 3.40 mm (λ_z = 0.81) by fixing their height after the second crosslinking process. This uniaxial compression (biaxial deformation) is the key step of the preparation process for the alignment of the sample, and together with the crosslinking density, will define the final expansion ratio of the LCE micropillars. In the nematic state, the LCE micropillars have average dimensions of 3.50 mm in height and 2.60 mm in diameter. After heating the LCE array to the isotropic phase, the average dimensions of the micropillars changed to 4.20 mm in height and 2.30 mm in diameter. This change in the LCE micropillar dimensions is directly connected to an increase in the order parameter of both the planar oriented polymer backbone and mesogens (S_p = −0.35 and S_m = −0.33, respectively) towards zero-values ($S_p = S_m = 0$) upon isotropization of the material.[22]

LCE micropillar mechanical analysis. In order to measure the mechanical actuation of the sample, the LCE micropillar array was heated from room temperature to 80 °C using a self-constructed miniaturized hotplate, which consisted of a Peltier TEC 1.4–6 from Thorlabs placed between two aluminum plates in order to stabilize and homogenize the temperature. Temperature was monitored by a temperature sensor ITC 510 from Thorlabs coupled to a power controller. The force generated during the expansion of the LCE micropillars when heated was measured using a dynamometer M5-025 from MARK9-10 with a resolution ΔF = 0.05 mN, which was in contact with the top surface of one single LCE micropillar. The use of a microtranslational stage allows the correct relative positioning between these elements. The resistors were connected to a DC power supplier DF1731SB5A from KaiseCorp., whereas the dynamometer was coupled to a computer, where a self-developed LabVIEW data acquisition interface was used in order to collect all relevant data like temperature, time and measured force. Moreover, a digital multimeter was used to verify the measurements.

LCE micropillar thermal analysis. The phase transformation behavior of the LCE micropillars was investigated by Differential Scanning Calorimetry (DSC) measurements using a Perkin Elmer DSC8500 differential scanning calorimeter equipped with a liquid nitrogen controller Cryofill at heating/cooling rates of dT/dt = 5, 10, and 20 K min^{-1}. The first order transition temperatures were determined by extrapolating the heating/cooling rate to 0 K min^{-1}. The glass transition temperature (T_g)

was determined by the half vitrification temperature ($1/2\Delta C_p$). The nematic-to-isotropic phase transformation temperature (T_{NI}) was determined by temperatures of the maxima of the heat flow. The changes in the heat capacity (ΔC_p) and the latent heat (ΔH_{NI}) were calculated from the thermograms.

LCE micropillar microscopy analysis. Changes in the micropillar dimensions as function of temperature or applied voltage were optically evaluated by means of an optical upright microscope DM LM from Leica. Movies of the expansion and recovery movements of the micropillars were recorded using a Moticam 2300 3.0 MPixels digital camera and later analyzed using ImageJ 1.50 software.

LCE micropillar temperature analysis. Infrared thermal measurements were carried out using a FLIR SC5500 infrared camera from Flir Systems equipped with InSb FPA detectors (320 × 256) and a G1 microscopic lens (30 μm-lateral resolution). All images were acquired at a frame rate of f = 376 Hz, and an integration time t_{int} = 301 μs. Temperature values on the surface of the LCE pillar were obtained assuming an emissivity value of 1.

LCE micropillar modeling. COMSOL Multiphysics software form Burlington, MA, was used for modelling the system by finite element methods. Thus, the evolution of both the temperature and the heat flux spatial distribution along the LCE micropillars were obtained as function of the voltage applied to the resistor, coupling both heat transfer and electric currents analysis modules, which are mainly based on the Joule effect in solids and the Fourier's and the first thermodynamic laws. The main properties of the LCE material and their variations according to the isotropization degree were considered. Detailed information of the modeling process can be found in the ESI.†

Results & discussion

LCE micropillar array's preparation and characterization

Constructing a LCE microdevice, which is switchable by controlling the amount of heat produced by a microresistor, requires for (i) the fabrication of the inorganic component based on standard Microsystems Technology knowledge, and (ii) the integration of the organic component based on liquid-crystalline materials. In the following, the fabrication process for the obtaining of Au-microresistors as heating units and the integration of LCE micropillar on top is described for the construction of a LCE micropillar array device.

For the actuation of the LCE micropillars, individual Au-microresistors of 1.5 mm × 1.5 mm were designed to be partially embedded into the LCE material helping the thermal actuation, resulting in a fast and uniform response. The fabrication process for the Au-microresistors based on lift-off technique is shown in Fig. 1A.[30] A 1.8 μm-thick photoresist layer was spin-coated on top of 700 μm-thick Pyrex wafer to be used as a sacrificial layer (step I). Then, a standard photolithographic process was performed in order to transfer the photomask pattern (microresistors layout) to the photoresist (step II), and a 50 nm-thick Au layer was sputtered on top (step III). Finally, the photoresist was washed out, lifting-off the non-desired parts of Au, leading to the microresistors (step IV).

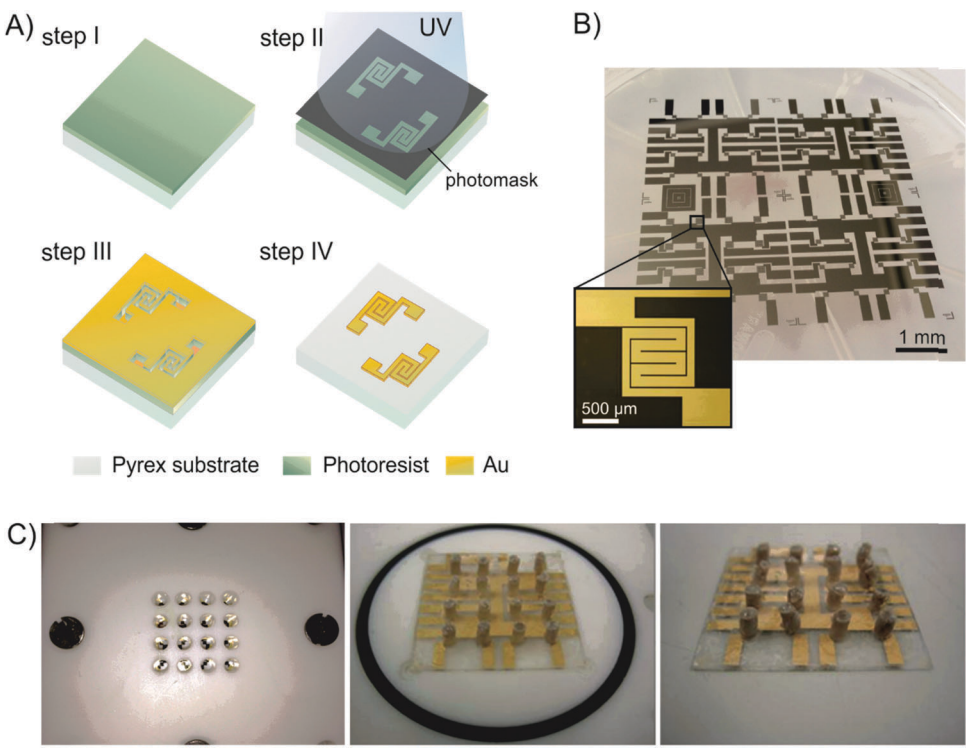

Fig. 1 (A) Fabrication of the Au-microresistors using standard Microsystems Technology. (B) Image of the processed Au-microresistor array on the handle Pyrex wafer with a detailed view. (C) Image sequence showing the fabrication of the LCE micropillar array on top of the Au-microresistors.

To improve the adherence of the Au-layer onto the Pyrex substrate, 10 nm-thick titanium–nickel (Ti–Ni) bilayer was previously deposited. Fig. 1B shows the array of microresistors once fabricated with their corresponding tracks and pads for the electrical connections, together with a detail of their geometry. In each processed wafer, four 30 mm × 30 mm chips containing an array of 4 × 4 Au-microresistors were obtained.

The surface chip containing the array of Au-microresistors was treated with a reactive silane (allyltrichlorosilane) in order to guarantee good chemical adhesion between both the LCE material and the Pyrex substrate, as well as to protect the Au-layer. Afterwards, it was placed inside the designed Teflon mold to define the shape and distribution of the micropillars forming the array[22] in a way that the Au-microresistors' centers coincided with the centers of the holds in the mold, and resulting in one microresistor for each single micropillar. The resulting LCE micropillar array device is shown in Fig. 1C, from the already integrated set of LCE micropillars after the first crosslinking step to the deswollen and already oriented active components.

For the fabrication and *in situ* integration of the liquid-crystalline actuators, a siloxane-based polymeric material – poly(methylhydrosiloxane), PMHS, with the corresponding nematic mesogen and crosslinker was synthesized (Fig. 2A) as described in previous papers.[22,25,27] The resulting nematic network showed low power requirements ($T_g < 0$ °C; $T_{NI} < 80$ °C), allowing for deformations of the whole sample and relatively high actuation forces. The orientated nematic LCE micropillar array was prepared using the new orientational process,[22] where both the mesogens and the polymer backbone show a planar orientation. The mixture of mesogen, crosslinker, polymer backbone, and catalyst in toluene was placed in the reactor/mold gaps, and removed after the non-complete hydrosilylation reaction at 70 °C. The sample was partially deswollen and removed from the reactor/mold, and aligned by imposing a uniaxial compression (biaxial deformation) in the direction of the cylindrical micropillar axis. The curing process allowed the completion of the hydrosilylation reaction, while maintaining the compression of the sample – second step of the crosslinking reaction – in the isotropic phase at 70 °C during the orientation of the sample.

Using this deformation approach, a two-dimensional prolate polydomain conformation of the polymer backbone together with the mesogens was obtained, which corresponds to a preferred planar orientation (Fig. 2B). Thus, when isotropization of the nematic LCE material takes place, an expansion along the direction where the uniaxial compression was applied and a contraction in the other two directions perpendicular to the applied deformation direction will be measurable. In contrast to the conventional uniaxially oriented prolate LCE materials, the two-dimensional prolate polydomains of LCEs obtained by uniaxial compression (or an equivalent biaxial orientation) induce an expansion along the macroscopic deformation direction. The actuation principle for the LCE micropillars consists of using an external stimulus to induce an expansion along the cylinder axis (λ_z) and shrinkage in the

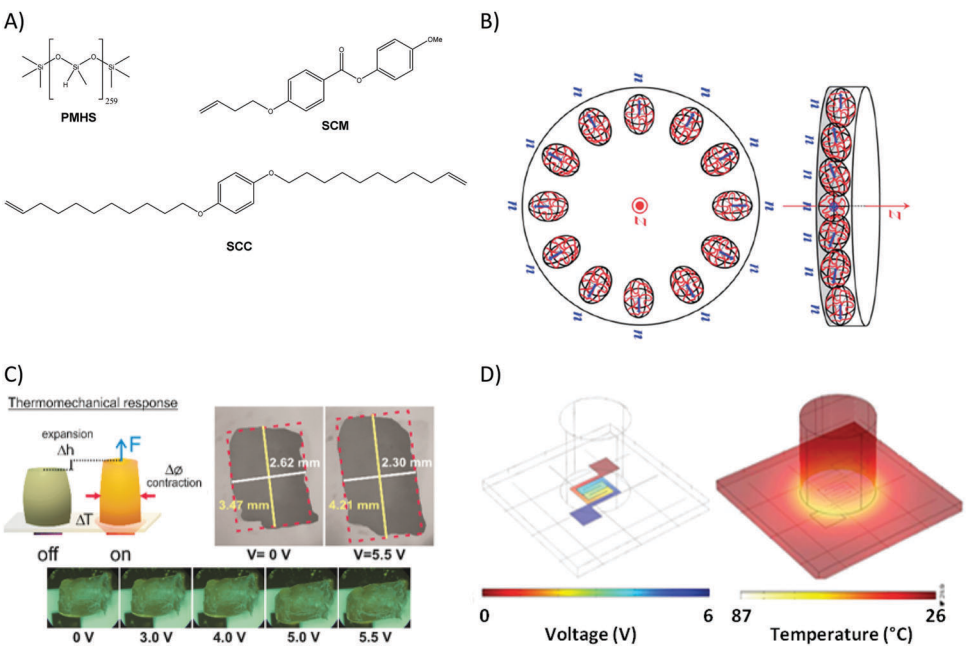

Fig. 2 (A) Chemical components for the synthesis of the LCE material and the later fabrication of the actuators. (B) Schematics of the planar (radial) orientation of the mesogens and the polymer backbone reached during the fabrication of the micropillars. Such a 2D distribution of prolate polymer backbone and nematic domains (polydomain) is perpendicular to the cylindrical axis of the LCE-micropillar (*z*-axis). (C) Thermo-mechanical principle due to uniaxial thermal expansion along the cylinder axis when electrical voltage is applied. The bottom series of light microscopy pictures shows the thermal expansion along the cylinder axis upon heating the LCE micropillar when increasing the voltage from 0 to 5.5 V. (D) Electric current distribution upon applying a voltage of 6 V (left), and temperature distribution along the Au-microresistor for heating the LCE micropillar base (right) obtained by Finite Element Modeling (FEM).

radial direction (λ_r), as shown from the thermoelastic experiment conducted on an oriented LCE micropillar (Fig. ESI-1, ESI†).

After the LCE micropillars alignment and final crosslinking, the demolded LCE micropillars with the embedded microresistors had a diameter of about 2.62 mm and 3.47 mm length (Fig. 2C), and a heater resistance of 104 Ω ± 0.1 Ω (Fig. ESI-2, ESI†). A sequence of images in Fig. 2C evidenced those shape changes on a LCE micropillar as function of the applied voltage, from which the corresponding uniaxial thermal expansion and contraction coefficients were evaluated. As expected, from 4.0 V the expansion of the micropillar along the axial direction became clearer, reaching the maximum expansion of ε_z = 21% (λ_z = 0.82) at around 5.5 V, with the corresponding contraction in the radial direction of ε_r = 12% (λ_r = 1.14) as evidenced from the thermoelastic experiment (Fig. ESI-1, ESI†). Fitting the experimental data with a heuristic formula, the clearing temperature (T_{NI} = 60.7 °C) could be estimated from the corresponding inflection point in the curve. The shape of such profile clearly indicated that such two-dimensional prolate polydomain conformation of the side-chain LCE micropillar has a supercritical transition behavior.[31–34]

Finite element modeling (FEM) is a powerful tool for the design and optimization of devices, as well as for response prediction, and is commonly used in Engineering and in Microsystems Technology. In order to properly adjust the testing parameters and predict the response of the device – Au-microresistors plus LCE micropillars, computer simulations were performed using COMSOL Multiphysics software (Burlington, MA, USA). Thus, an accurate model was created coupling both electric current and heat transfer analysis modules.

Briefly, in order to obtain the heat flux distribution along the LCE microdevice, a single Au-microresistor plus a LCE micropillar was modeled coupling heat transfer and electric currents modules, which are mainly based on the Joule effect in solids and on the Fourier's and the first thermodynamic laws, for a transient analysis. The main properties of the LCE material and their variations according to the isotropization degree, *i.e.*, ΔC_P and ΔH, as well as changes on the resistivity of Au under the application of voltage were considered from experimental results. For an accurate analysis, thermal dissipation losses due to the contacts between both materials and the substrate, and convection effects with the surrounding air were also implemented on the model. Details of the modeling procedure and the main steps applied can be found in the ESI.†

Fig. 2D shows the electric current distribution upon applying a voltage of 6 V (left), and the temperature distribution (right) resulting from the simulation of a single Au-microresistor and the entire LCE microdevice – Au-microresistor plus the LCE micropillar, respectively, according to the conditions previously described. When an electric potential difference of 6 V is applied between the terminals of the resistor (Fig. 2D-left), the Au layer heats up rapidly due to the Joule effect, transmitting part of the generated heat to the base of the LCE micropillar (Fig. 2D-right).

The thermal properties of the LCE micropillars were evaluated by performing DSC experiments, showing a glass transition temperature T_g = −8 °C with a change in the heat capacity of ΔC_p = 0.420 J K^{-1} g^{-1} – characteristic of polysiloxane-based LCEs, and a clearing temperature of T_{NI} = 59 °C with a transition enthalpy of ΔH_{NI} = 1.13 J g^{-1} – common for nematic elastomers – (Fig. 3A). It has to be noted that the isotropization temperature (T_{NI}) was determined by extrapolating the values obtained from the heating/cooling rate to 0 K min^{-1}, thus fast heating processes will show clearing temperatures at higher values, *e.g.*, 64 °C at 20 K min^{-1}.

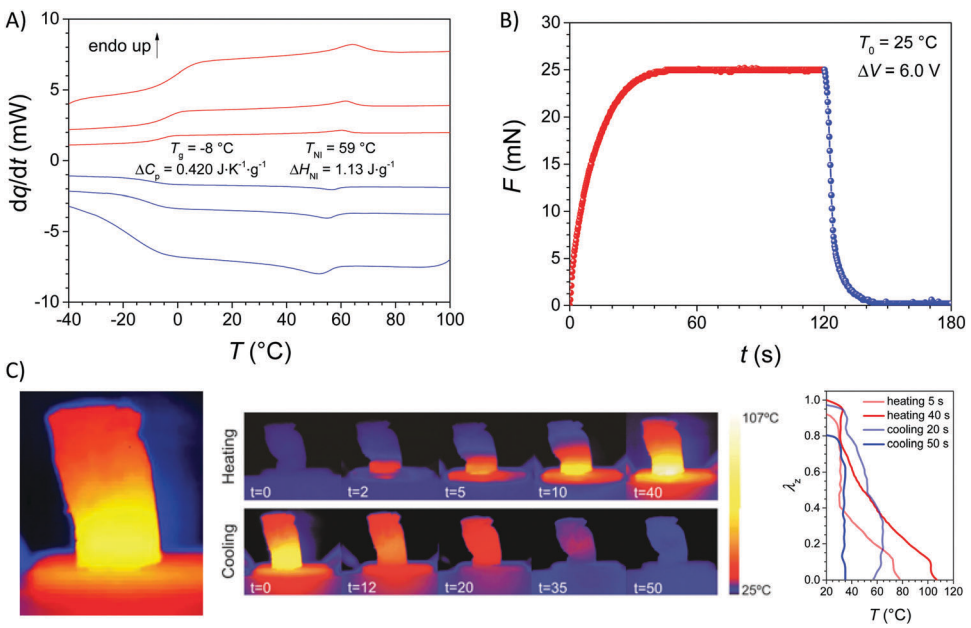

Fig. 3 (A) DSC thermograms of the crosslinked LCE material at different heating and cooling rates. (B) Actuation curves showing the main heating (red curve) and cooling (blue curve) processes with a maximal actuation force of F = 25 mN. (C) Temperature evolution along the LCE micropillar's height as function of time for both heating and cooling cycles with the corresponding temperature profiles at 5 and 40 s heating and at 20 and 50 s cooling. Temperature values experimentally measured by IR camera (scale bar = 1 mm).

These temperature values evidenced that the material was suitable for actuation because of having a soft and flexible polymer backbone with a relatively low actuation temperature.

Preliminary mechanical testing of a LCE micropillar showed a relatively fast response after applying 6 V of electrical voltage at 25 °C as shown in Fig. 3B. The heating red curve showed a full isotropization – 99% of the maximum force of $F = 25$ mN – of the LCE micropillar after 45 s, while the cooling blue curve indicated that only 25 s were needed for the full recovery of the sample. From the resulting force value obtained upon reaching the plateau, a full description of the mechanical response of such LCE micropillars at different applied voltage values was constructed. Thus, combining image processing and force measurements allows for the evaluation of both stress (σ) and expansion along the cylinder axis (λ_z) at different electrical voltage values (Fig. ESI-3, ESI†). The results show a maximum force of *ca.* 20 mN, which corresponds to a stress value of *ca.* 6 kPa at $\lambda_z = 1$.

Temperature evolution along the LCE micropillar's height as function of time was evaluated experimentally using an IR camera upon applying a voltage of 6 V. Fig. 3C shows the temperature profile at the surface of the LCE micropillar at different heating and cooling times, proving the direct transfer of the generated heat in the Au-microresistor to the LCE material. From the temperature profile analysis during the heating process (Fig. ESI-4A, ESI†), heat transferred from the Au-microresistor to the base of the LCE Micropillar is observed, and accumulates in the LCE bulk material even that some heat is lost *via* convection with the surrounding air. After stopping the applied voltage (Fig. ESI-4B, ESI†), the accumulated heat in the LCE micropillar is transferred *via* convection to the setup air atmosphere and *via* conduction to the Pyrex-support element below the LCE Micropillar. The cooling behavior of the LCE micropillar is controlled by the thermal properties of the microdevice elements: the LCE micropillar diffuses heat slower than the support, thus a maximum in the temperature profile right above to the LCE micropillar base is observed.

LCE micropillar array's mechanical response

First mechanical experiments on five LCE micropillars were performed in order to obtain the characteristics of such LCE materials. The LCE micropillar array device was placed in a closed chamber, which initial temperature (T_0) was controlled by a Peltier system, and the pushing force (F) was measured when putting in contact the dynamometer to the top of a LCE micropillar after applying a square wave electrical voltage (V) as shown in Fig. 4A and Fig. ESI-5 (ESI†). Each set of data at the same initial temperature was fitted with a heuristic formula related to a sigmoidal function – Boltzmann (eqn (1)), which allowed for the estimation of the required voltage for the isotropization of the LCE micropillar (V_{NI}) corresponding to the inflection point of the fitting curve (Table ESI-1, ESI†).

$$F(V) = F_0 + \frac{\Delta F}{1 + e^{\frac{V - V_{NI}}{dV}}} \quad (1)$$

The initial force (F_0) obtained from each set of data at different initial temperature (T_0) also allowed for the construction

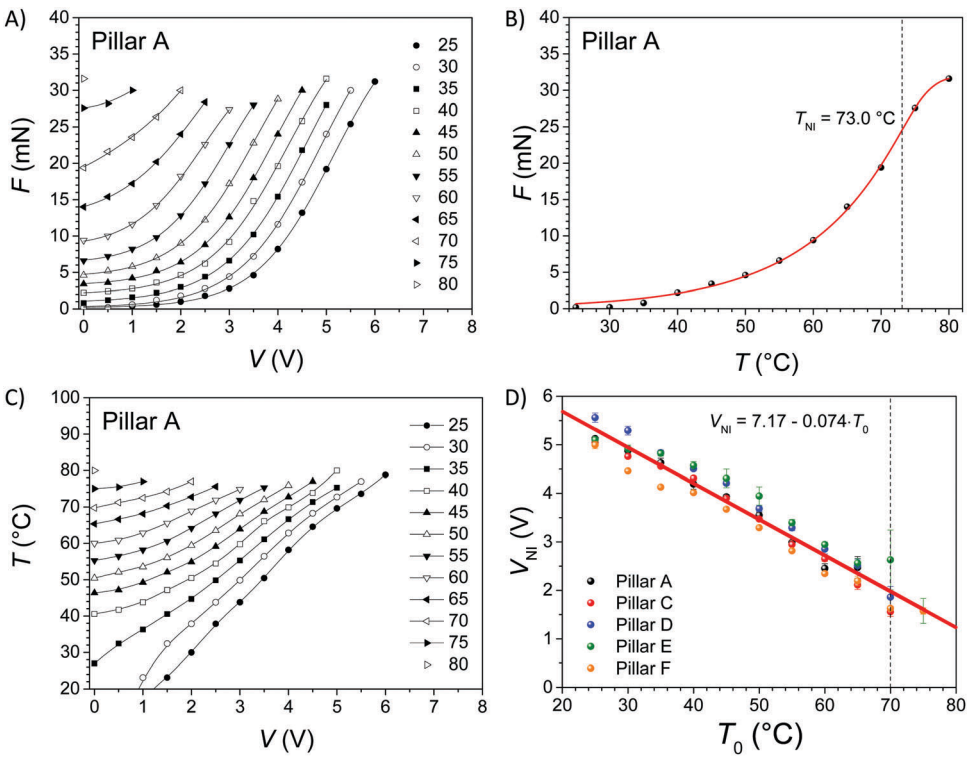

Fig. 4 (A) Force (F) as function of the applied square wave voltage (V) at different initial temperatures (T_0). Note: a maximal actuation force of $F = 32$ mN was measured for this LCE micropillar (B) force (F) as function of temperature (T). (C) Temperature (T) as function of the applied square wave voltage (V) at different initial temperatures (T_0). (D) Required voltage for the isotropization (V_{NI}) of the pillar as function of the initial temperature (T_0) for 5 different pillars analyzed.

of a force–temperature plot (Fig. 4B and Fig. ESI-6, ESI†). After fitting with a heuristic formula related to a sigmoidal function – Richards (eqn (2)), the isotropization temperature for the LCE micropillar (T_{NI}) was obtained, which corresponded to the inflection point of the fitting curve (Table ESI-1, ESI†).

$$F(T) = a\left[1 + b\mathrm{e}^{-c(T-T_{NI})}\right]^{-\frac{1}{b}} \quad (2)$$

Thanks to the inverse function $F^{-1}(T)$ of the previous fitting curve (eqn (2)) in Fig. 4B, all force values (F) were translated into temperature values $T(F)$, and a temperature–voltage curve (Fig. 4C and Fig. ESI-7, ESI†) could be constructed and used further for determining force–temperature–voltage relationships. Moreover, this transformation enabled for the determination of the LCE micropillar temperature when knowing the applied voltage (V) and initial temperature (T_0).

Finally, by plotting the isotropization voltage (V_{NI}) as function of the initial temperature (T_0), a linear relationship was observed (Fig. 4D) showing that a lower voltage is needed for the isotropization of the LCE micropillar array when closer the initial temperature is to the nematic-to-isotropic transition. Thus, the applied voltage for the nematic-to-isotropic transition ranges from 5.32 V at 25 °C to 1.98 V at 70 °C.

After determining the most relevant parameter related to the mechanical response of the LCE micropillar array, time-dependent experiment were performed upon applying a square wave voltage to the Au-microresistor using three different setups (Fig. ESI-8, ESI†). Setup 1 is a closed system, which temperature is controlled by a Peltier system in direct contact to the bottom Pyrex surface (“Closed Chamber/Peltier” experiments). Setup 2 corresponds to the same assembly that the one for setup 1 but without controlling the temperature with the Peltier block (“Closed Chamber” experiments). Finally, setup 3 is an open system where the LCE microdevice is insulated from the Peltier-heating block (“Open Chamber” experiments).

First time-dependent experiments were conducted by using the “Closed Chamber/Peltier” setup 1, where an initial temperature (T_0) controlled by a Peltier system was imposed followed by applying a square wave voltage (V) in order to bring the nematic micropillar to the isotropic state. In this way, the pushing force (F) of the micropillar was monitored as shown in Fig. 5A and Fig. ESI-9 (ESI†). Experimental data were fitted with two stretched exponential growth functions (eqn (3)) for the heating process (Fig. 5A and Fig. ESI-10, red curve, ESI†),

$$\frac{F}{F_{max}} = \left(\frac{F_{h0}}{F_{max}}\right) + A\left[\mu\left(1 - \mathrm{e}^{-\left(\frac{t-t_0}{\tau_{h1}}\right)^{\beta_{h1}}}\right) + (1-\mu)\left(1 - \mathrm{e}^{-\left(\frac{t-t_0}{\tau_{h2}}\right)^{\beta_{h2}}}\right)\right] \quad (3)$$

where μ, τ_{h1} and β_{h1} and $(1-\mu)$, τ_{h2} and β_{h2} are the population, lifetime and stretched exponent for the fast and slow process, respectively, upon heating the device. It is worth mentioning

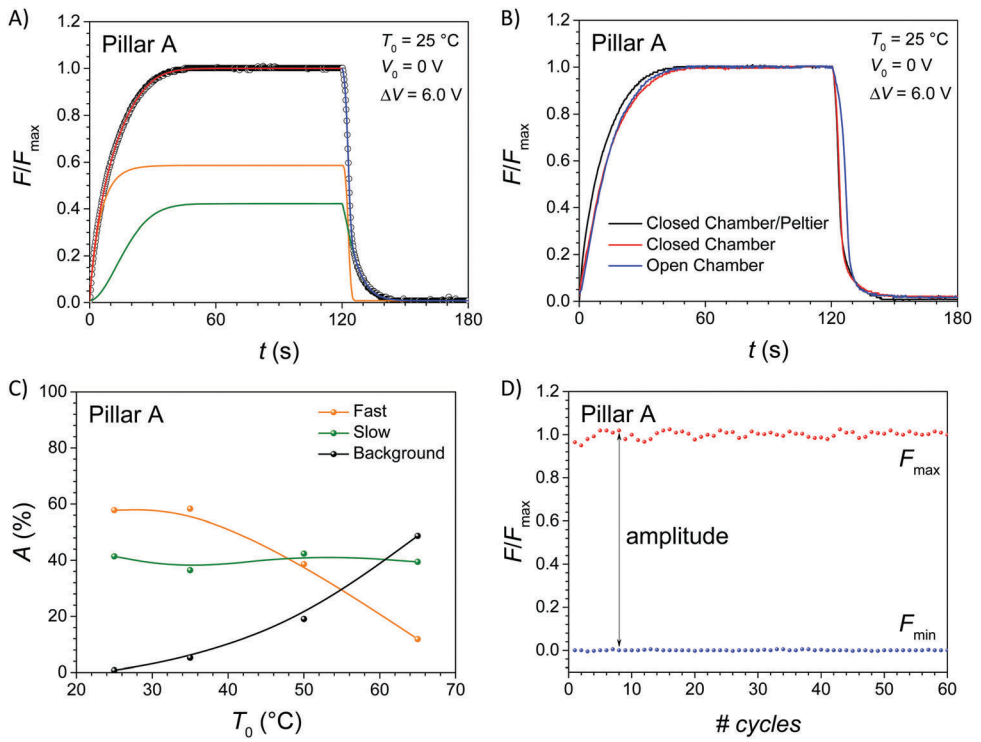

Fig. 5 (A) Force evolution (F/F_{max}) upon applying a voltage (ΔV) of 6.0 V for 120 s at 25 °C, and after removal of the voltage, as well as the corresponding fitting curves for the heating and cooling processes. (B) Comparison of the three methods used for heating the pillar. (C) Mechanical contribution (A) for the fast and slow process, and the thermally induced background force as function of the initial temperature (T_0). (D) Reproducibility of LCE micropillar actuation during several heating and cooling cycles.

that neither two normal exponential growth functions nor one stretched exponential function could fit the experimental data. Stretched exponential functions can be understood as a sum of exponential functions. Thus, we assume that heat transfer takes place through the sample from the bottom part of the LCE micropillar to the top, and a continuous force profile is axially distributed along the cylindrical direction of the LCE micropillar. The resulting pushing force is an average force obtained between the hottest and the coldest regions along the z-axis, and can eventually be explained by using stretched exponential functions where values for the stretch exponent $0 < \beta < 1$ and $\beta > 1$ correspond to a faster (stretched) and a slower (compressed) process, respectively, compared to the normal exponential function ($\beta = 1$).

A similar procedure was implemented for the fitting of the experimental data after removal of the applied voltage. In this case, two stretched exponential decay functions (eqn (4)) were used for describing the cooling process (Fig. 5A and Fig. ESI-10 (ESI†), blue curve),

$$\frac{F}{F_{\max}} = \left(\frac{F_{c0}}{F_{\max}}\right) + A\left[\mu e^{-\left(\frac{t-t_0}{\tau_{c1}}\right)^{\beta_{c1}}} + (1-\mu)e^{-\left(\frac{t-t_0}{\tau_{c2}}\right)^{\beta_{c2}}}\right] \quad (4)$$

where μ, τ_{c1} and β_{c1} and $(1-\mu)$, τ_{c2} and β_{c2} are the population, lifetime and stretched exponent for the fast and slow process, respectively, upon cooling the device.

The same LCE micropillar was studied with the other two setups (setup 2: Fig. ESI-11 and 12; setup 3: Fig. ESI-13 and 14, ESI†). The results obtained from fitting both the heating and cooling process for the three different setups are summarized in Tables ESI-2–4 (ESI†). From the fitting of the experimental data a fast (Fig. 5A and Fig. ESI-10, 12 and 14, orange curve, ESI†) and a slow (Fig. 5A and Fig. ESI-10, 12 and 14, green curve, ESI†) were identified. The fast process could be related to the energy accumulation in the LCE micropillar (small diffusivity coefficient of this material), which percentage decreases upon increasing the temperature, while the slow process could be described by the viscoelastic response of the material, which forces to rearrange all components in the LCE matrix. Basically, the average time needed in order to achieve 90% of the maximum response upon heating for both the fast and slow process was $t_{0.90}$(fast) = 13, 26 and 18 s and $t_{0.90}$(slow) = 30, 34 and 33 s – which corresponding lifetime values are τ_{h1}(fast) = 5, 13 and 8 s and τ_{h2}(slow) = 18, 16 and 19 s – for the experiments performed with setup 1, 2 and 3, respectively. Setup 1 transfers heat faster than the other two setups due to the Peltier system, and setup 3 minimizes the loss of heat due to the insulation of the LCE microdevice with respect to the block system. Moreover, the fast process is twice as faster than the slow process. The analysis for the evaluation of the cooling process brings average response times of $t_{0.90}$(fast) = 5, 6 and 10 s and $t_{0.90}$(slow) = 16, 18 and 16 s – lifetime values of τ_{c1}(fast) = 4, 5 and 9 s and τ_{c2}(slow) = 8, 8 and 9 s – for the experiments conducted with setup 1, 2 and 3, respectively. In this case, the setup 1 and 2 dissipate better heat contributing to a faster cooling process that the one observed for setup 3 which the only mean of heat dissipation is the surrounding air. Moreover, upon heating and cooling, the fast process is as fast as twice and three times, respectively, the speed of the slow process with deviations depending on the setup used. Fig. 5B depicts a comparison between the different responses of the LCE microdevice as function of the measuring setup used at 25 °C, showing that setup 1 is faster than setup 3, which is faster than setup 2, upon heating, and setup 1 and 2 are faster than setup 3 upon cooling.

Another point to discuss is the contribution to the total mechanical response of such a fast and slow process during the actuation and relaxation mode of the LCE microdevice. Fig. 5C clearly explains how the percentage contribution of the fast process (orange data points) is temperature dependent, and the corresponding decrease in percentage is taken over by the background mechanical response (black data points), which refers to the offset force value due to the imposed initial temperature (T_0). Thus, the compensation between these two mechanical contributions makes the slow process (green data points) almost constant among the range of temperatures studied.

Repeatability and feasibility of the micropillars actuation were evaluated by means of several cyclic actuation tests. An example is illustrated in Fig. 5D, where 60 cycles were studied resulting in a constant force amplitude of $F_{\max}$ = 20.1 mN ± 0.3 mN with no significant variation (σ = 1.6%). Further experiments on another micropillar (Fig. ESI-15, ESI†) during five on/off actuation cycles where 5.5 V were applied showed a fully reversible process of maximum actuation force of $F_{\max}$ = 19.4 mN ± 0.4 mN.

Conclusions

A new heat-controlled LCE micropillar array device with two-dimensional prolate polydomain conformation of the polymer backbone and the mesogens has been successfully produced. The macroscopic change in shape of the LCE micropillars is controlled by the resulting heat (Joule effect) produced when a voltage is applied to the Au-microresistors at the base of each LCE micropillar. Such micropillars show a maximum expansion of ε_z = 21% (λ_z = 0.82) along the axial direction and a contraction of ε_r = 12% (λ_r = 1.14) in the radial direction upon isotropization of the sample. These changes in the dimensions produce a maximal actuation force of F = 32 mN (σ = 9.6 kPa) when fully isotropic (λ_z = 1).

Time-dependent experiments were performed upon applying a square wave voltage to the Au-microresistor using three different setups, and the LCE micropillar force evolution monitored in different conditions. The analysis of the resulting actuation as function of time reveals the presence of a fast (energy uptake) and a slow (viscoelastic response) process when heating and cooling the system. The times needed for achieving the isotropic state and come back to the nematic phase is *ca.* 30 s and 20 s, respectively, which corresponds to lifetime values of 5 s (fast process) and 16 s (slow process) and of 4 s (fast process) and 8 s (slow process) upon heating and cooling the

LCE microdevice, respectively. Such actuation time is much faster than the previous LCE microdevice[1,13–23] – and similar to other LCE systems[35] – due to the improvement in the LCE microdevice fabrication and control in the heat transfer by the use of Au-microresistors in order to reach the isotropic state.

Such combination of Microsystems Technology and Smart Materials, *e.g.*, LCEs, makes LCE microdevices suitable candidates for haptic applications and for the development of complex devices through a batch process.

Conflicts of interest

There are no conflicts to declare.

Acknowledgements

Authors want to thank Dr Miquel Vellvehí from IMB-CNM for his help in the experiments with the IR camera, Edgardo Leon Salguero from IMB-CNM and Universidad de Sonora for assisting us in the LCE micropillar modeling with COMSOL Multiphysics software, as well as the Clean Room staff from IMB-CNM for the fabrication of the Au-microresistors. Finally, authors want to thank Prof. Philippe Martinoty for his unconditional support and critical reading of this work.

References

1 A. Sánchez-Ferrer, N. Torras and J. Esteve, in *Integration of Liquid-Crystalline Elastomers in MEMS/MEOMS, in Liquid Crystalline Polymers: Structure and Chemistry*, ed. V. K. Thakur and M. R. Kessler, Springer International Publishing, 2015, ch. 19.
2 M. Warner and E. M. Terentjev, *Liquid Crystal Elastomers*, Clarendon, Oxford, revised edition, 2007.
3 M. Camacho-López, H. Finkelmann, P. Palffy-Muhoray and M. Shelley, *Nat. Mater.*, 2004, **3**, 307.
4 A. Sánchez-Ferrer, A. Merekalov and H. Finkelmann, *Macromol. Rapid Commun.*, 2011, **32**, 672.
5 A. Kaiser, M. Winkler, S. Krause, H. Finkelmann and A. M. Schmidt, *J. Mater. Chem.*, 2009, **19**, 538.
6 J. M. Haberl, A. Sánchez-Ferrer, A. M. Mihut, H. Dietsch, A. Hirt and R. Mezzenga, *Adv. Mater.*, 2013, **25**, 1787.
7 M. Chambers, H. Finkelmann, M. Remskar, A. Sánchez-Ferrer, B. Zalar and S. Zumer, *J. Mater. Chem.*, 2009, **19**, 1524.
8 T. Hiscock, M. Warner and P. Palffy-Muhoray, *J. Appl. Phys.*, 2011, **109**, 104506.
9 P. G. de Gennes, *C. R. Seances Acad. Sci., Ser. B*, 1975, **281**, 101.
10 H. Finkelmann, H. J. Kock and G. Rehage, *Macromol. Rapid Commun.*, 1981, **2**, 317.
11 Y. Ji, Y. Y. Huang, R. Rungsawang and E. M. Terentjev, *Adv. Mater.*, 2010, **22**, 3436.
12 J. M. Haberl, A. Sánchez-Ferrer, A. M. Mihut, H. Dietsch, A. M. Hirt and R. Mezzenga, *Adv. Funct. Mater.*, 2014, **24**, 3179.
13 M. Bründel, M. Stubenrauch, H. Wurmus and A. Sánchez-Ferrer, *Int. Newslett. Micro-Nano Integr. (MSTNEWS)*, 2004, **4**, 38.
14 M. Yamada, M. Kondo, J. Mamiya, Y. Yu, M. Kinoshita, C. J. Barret and T. Ikeda, *Angew. Chem., Int. Ed.*, 2008, **47**, 4986.
15 A. Sánchez-Ferrer, T. Fischl, M. Stubenrauch, H. Wurmus, M. Hoffmann and H. Finkelmann, *Macromol. Chem. Phys.*, 2009, **210**, 1671.
16 M. Chen, X. Xing, Z. Liu, Y. Zhu, H. Liu, Y. Yu and F. Cheng, *Appl. Phys. A: Mater. Sci. Process.*, 2010, **100**, 39.
17 A. Sánchez-Ferrer, T. Fischl, M. Stubenrauch, A. Albrecht, H. Wurmus, M. Hoffmann and H. Finkelmann, *Adv. Mater.*, 2011, **23**, 4526.
18 N. Torras, K. E. Zinoviev, C. J. Camargo, E. M. Campo, H. Campanella, J. Esteve, J. E. Marshall, E. M. Terentjev, M. Omastova, I. Krupa, P. Teplicky, B. Mamojka, P. Bruns, B. Roeder, M. Vallribera, R. Malet, S. Zuffanelli, V. Soler, J. Roig, N. Walker, D. Wenn, F. Vossen and F. M. H. Crompvoets, *Sens. Actuators, A*, 2014, **208**, 104.
19 A. Buguin, M. H. Li, P. Silberzan, B. Ladoux and P. Keller, *J. Am. Chem. Soc.*, 2006, **128**, 1088.
20 C. J. Camargo, H. Campanella, J. E. Marshall, N. Torras, K. Zinoviev, E. M. Terentjev and J. Esteve, *J. Micromech. Microeng.*, 2012, **22**, 075009.
21 Y. Jiang, Y. D. Xu, L. Xuesong, C. Lin, W. Li, Q. An, C. Tao, H. Tang and G. Li, *J. Mater. Chem.*, 2012, **22**, 11943.
22 N. Torras, K. E. Zinoviev, J. Esteve and A. Sánchez-Ferrer, *J. Mater. Chem. C*, 2013, **1**, 5183.
23 S. Schuhladen, F. Preller, R. Richard, S. Petsch, R. Zentel and H. Zappe, *Adv. Mater.*, 2014, **26**, 7247.
24 H. Finkelmann, U. Kiechle and G. Rehage, *Mol. Cryst. Liq. Cryst.*, 1983, **94**, 343.
25 J. Küpfer and H. Finkelmann, *Makromol. Chem., Rapid Commun.*, 1991, **12**, 717.
26 J. Küpfer and H. Finkelmann, *Macromol. Chem. Phys.*, 1994, **195**, 1353.
27 H. Finkelmann, A. Greve and M. Warner, *Eur. Phys. J. E: Soft Matter Biol. Phys.*, 2001, **5**, 281.
28 W. Caseri and P. S. Pregosin, *Organometallics*, 1988, **7**, 1373.
29 B. Marciniec, *Comprehensive Handbook on Hydrosilylation*, Pergamon, Oxford, 1992.
30 S. A. Campbell, *Fabrication Engineering at the Micro- and Nanoscale*, New York, Oxford University Press, 3rd edn, 2008.
31 J. V. Selinger, H. G. Jeon and B. R. Ratna, *Phys. Rev. Lett.*, 2002, **89**, 225701.
32 A. Lebar, Z. Kutnjak, S. Žumer, H. Finkelmann, A. Sánchez-Ferrer and B. Zalar, *Phys. Rev. Lett.*, 2005, **94**, 197801.
33 G. Cordoyiannis, A. Lebar, B. Zalar, S. Zumer, H. Finkelmann and Z. Kutnjak, *Phys. Rev. Lett.*, 2007, **99**, 197801.
34 G. Cordoyiannis, A. Sánchez-Ferrer, H. Finkelmann, B. Rozic, S. Zumer and Z. Kutnjak, *Liq. Cryst.*, 2010, **37**, 349.
35 S. Petsch, R. Rix, B. Khatri, S. Schuhladen, P. Müller, R. Zentel and H. Zappe, *Sens. Actuators, A*, 2015, **231**, 44.

